Published in final edited form as:
Nat Nanotechnol. 2019 February ; 14(2): 184–190. doi:10.1038/s41565-018-0336-3.

Binding to Nanopatterned Antigens is Dominated by the Spatial Tolerance of Antibodies

Alan Shaw[1], **Ian T Hoffecker**[1], **Ioanna Smyrlaki**[1], **Joao Rosa**[1], **Algridas Grevys**[2,3,6], **Diane Bratlie**[4], **Inger Sandlie**[2,3], **Terje Enar Michaelsen**[4,5], **Jan Terje Andersen**[2,6], and **Björn Högberg**[1,*]

[1]Dept. of Medical Biochemistry and Biophysics, Karolinska Institutet, S-17177 Stockholm, Sweden

[2]Centre for Immune Regulation (CIR), Dept. of Immunology, Oslo University Hospital Rikshospitalet, University of Oslo, N-0424 Oslo, Norway

[3]CIR, Department of Biosciences, University of Oslo, N-0371 Oslo, Norway

[4]Dept. of Infectious Disease Immunology, Norwegian Institute of Public Health, N-0403 Oslo, Norway

[5]School of Pharmacy, University of Oslo, N-0403 Oslo, Norway

[6]Dept. of Pharmacology, Institute of Clinical Medicine, University of Oslo and Oslo University Hospital, 0424 Oslo, Norway

Abstract

Although repetitive patterns of antigens are crucial for certain immune responses, an understanding of how antibodies bind and dynamically interact with various spatial arrangements of molecules is lacking. Hence, we introduce a new method where molecularly precise nanoscale patterns of antigens are displayed using DNA origami and immobilized in a surface plasmon resonance (SPR) setup. Using antibodies with identical antigen binding domains, we find that all subclasses and isotypes studied, bind bivalently to two antigens separated at distances ranging from 3 to 17 nm. The binding affinities of these antibodies change with the antigen distances, with a distinct preference for antigens separated by approximately 16 nm, and considerable differences in spatial tolerance exist between IgM and IgG and between low and high affinity antibodies.

*Correspondence to: bjorn.hogberg@ki.se.

Author Contributions. AS, JTA and BH conceived the study and wrote the paper. JTA, IngSa, AG and TEM helped conceive the human antibody panel study. AS performed most of the experimental work on origami and SPR. IH performed most of the theoretical and modelling work. IoSmy performed a significant proportion of the experimental work on origami and SPR. JR performed origami experiments and design. JTA, DB, TEM and AG performed production and purification of the human Ab variants. All authors contributed to writing the manuscript.

Data availability. The raw data that support the plots within this paper and other findings of this study are provided in Supplementary Information and are available from the authors upon reasonable request.

Europe PMC Funders Author Manuscripts

Introduction

Rigidly organized molecular patterns are typically either foreign or intracellular in most mammals and the immune system has thus evolved an efficient response to such structures1. In fact, the concept of particulate antigen display has been successfully exploited for vaccine development2,3. (See also Supplementary Note 1) Exactly how such patterns elicit a strong response is however still not fully understood. A recent study using high speed atomic force microscopy (AFM) has suggested that antibodies (Abs), and thus also by extension B-cell receptors (BCRs), are able to 'walk' on a pattern of antigens by attachment and release of its Fab arms4. This concept, combined with a clustering model of BCR activation5, could provide more clues as to why B-cell activation is strong for rigid and highly organized patterns of antigens. Whatever the case may be, a picture is nevertheless emerging where it is becoming clear that deeper knowledge of the dynamics of Ab binding to variably distributed antigens would be highly desirable for a more complete understanding of the initiation of immune responses and for rational vaccine design.

Multivalent binding interaction between Abs and antigens is also regarded as one of the dominant modes to initiate antibody effector functions (Supplementary Note 1) such as complement activation6, Ab dependent cell-mediated cytotoxicity7, opsonophagocytosis and Ab-mediated antigen presentation8,9. Thus, the geometric organization of antigens not only plays an important role in influencing initiation but also on the induced Ab isotype and subclass effector functions.

Abs consist of two identical antigen binding fragment arms (Fab) and a constant fragment crystallizable region (Fc) (Fig. 1a, Supplementary Fig. 1) in a homodimeric molecule connected via disulfide bridges10. Humans have five Ab isotypes (IgM, IgD, IgG, IgE and IgA) where IgG, the most abundant in plasma, can further be divided into four subclasses (IgG1, IgG2, IgG3, and IgG4). Sequence differences between the Ab isotypes (Supplementary Figs. 1-2) result in several differences, for example the number of domains of their heavy chains and the makeup of the flexible hinge region located between the two Fabs and the Fc region. The human IgG subclasses have minor differences in amino acid composition in the Fc region, but have substantial differences in amino acid sequence and length of their hinge regions. These differences result in very distinct functional properties and engagement of Fc receptors and the complement system11. Crystal structures of full-length IgG are few10 (Supplementary Fig. 1) due to their flexibility6,12, but have revealed strikingly asymmetric conformations somewhere between a T- and a Y-shape. Electron microscopy has been used to estimate that IgG should be capable of bivalently binding antigens separated by 6-14 nm for mouse13 or human14 while fluorescence energy transfer studies suggest a slightly wider bivalent binding distance15.

Despite all clues to its importance, the answer to the question on how structural flexibility affects the ability of Abs to bind their cognate antigens at different distances and densities remains largely unknown. In particular no methods have been able to precisely show the optimal antigen separation required for the most stable bivalent bindings.

Design and Characterization of Patterned Surface Plasmon Resonance

In order to characterize the dynamic interplay between Ab structural flexibility and binding to cognate antigen patterns in real time, we applied DNA nanotechnology16 using DNA origami17–19, which has been used to arrange proteins or chemicals such as fluorophores, with nanometer20–23 or sub-nanometre precision24, including demonstrations of bivalent binding25. The method was established by conjugation of hapten (small molecule antigen) patterns to well-defined DNA origami nanostructures (Fig. 1b-d) that were immobilized on a surface plasmon resonance (SPR) chip using oligonucleotide hybridization (Fig. 1e-f). We designed two DNA origami nanostructures, an 18-helix bundle (18HB) and a brick used for pairwise distance measurements or multi-antigen 2D patterns, respectively, (Fig. 1d, Supplementary Figs. 3-6, Supplementary Table 1) patterned with either Digoxigenin (DIG), NIP (4-hydroxy-3-iodo-5-nitrophenylacetate) or NP (4-Hydroxy-3-nitrophenyl) antigens. The repertoire of human anti-NIP Abs with equivalent Fab affinities established previously (see Methods) constitute an opportunity to study and compare medically relevant classes of Abs and were used for the main experiments as far as possible with NP or NIP as antigens. To establish the method, and in particular when strong monovalent binding affinity was needed as in the case of complex binding patters, we resorted to the use of commercially available high affinity rabbit or mouse anti-DIG IgG. Serial dilutions of anti-hapten Abs were injected over stably immobilized DNA nanostructures and the obtained sensorgrams (single-cycle kinetics) (Fig. 1g) were fitted to a 1:1 Langmuir binding model to derive the binding constants (Supplementary Fig. 6-7). We refer to the method as Patterned SPR (pSPR).

To validate the robustness of the pSPR method, we took advantage of monoclonal mouse IgG1 and rabbit anti-Digoxigenin IgG Abs (Alignment data in Supplementary Fig. 8-9) and measured binding to origami patterns with Digoxigenin. The structures displaying widely spaced, monovalent binding inducing antigens, resulted in binding affinities in the range of K_D = 25-35 pM (apparent dissociation constant) where the binding occupancy scaled well with the number of antigens per structure (Supplementary Fig. 10 binding kinetics data given in Supplementary Table 2). ANOVA analysis showed that the location of the antigens on the monovalent nanostructure did not affect the binding interaction significantly (Supplementary Table 3). Nanostructures with two closely spaced hapten molecules showed a significant increase in binding affinity (approx. 10-fold decrease in K_D), with a binding occupancy of one Ab per structure, consistent with the formation of bivalent binding. Nanostructures with three antigens gained binding affinities in-between monovalent and bivalent binding, where the binding occupancy resulted in roughly two Abs per structure, indicating a mixture of monovalent and bivalent binding. Furthermore, we introduced some extra mobility to the antigens by increasing the linker length from 2 to 21 nucleotides (NT), which resulted in similar Ab binding patterns (Supplementary Fig. 11). Removing the 2-nucleotide linker, gave no significant difference in the Ab's binding affinity towards the 3.4 nm sample, suggesting that the uncertainty of distances between two antigens is smaller than the linker's contour length, probably due to the entropic-spring-like behaviour of both the linkers and the overall structural flexibility (Supplementary Fig. 12 and Methods). Small molecules displayed on origami constitute state-of-the-art molecular positioning, so while

distances can vary from fluctuations in individual structures, the ensemble average nature of our measurements over a large number of entropic springs, ensure robust comparisons over nanometre distances similarly to previous studies using origami distance measurements24,25. As the density of individual nanostructures on the SPR chip may influence the binding kinetics by allowing a single Ab to bridge two such neighbouring structures, we verified that the seeding density in our case did not influence the binding affinity for the concentrations of the structures used (Supplementary Fig. 13). Quantitative incorporation of hapten modified staples to the nanostructures is also key to the pSPR method, using gel retardation assays, we demonstrated that an undetectable amount of our nanostructures have defects in hapten oligo incorporation (Supplementary Figs. 4 and 14).

Exploring the Conformational Flexibility of Different Human IgG Subclasses

Next, we aimed to explore the conformational flexibility of the four human IgG subclasses by the use of mouse-human chimeric versions harbouring specificity for the hapten NIP (see Methods). Binding was studied using the 18HB on which two NIP molecules were arranged at distances ranging from 3 nm to 44 nm (Supplementary Fig. 6) and a monovalently decorated structure (denoted “0 nm”) (Fig. 2, Supplementary Table 4). We observed bivalent binding as a significant decrease (> 1500-fold) in the K_D for optimal distances compared to the monovalent samples. Interestingly, instead of a sharp cut-off between monovalent and bivalent binding, a u-shaped behaviour in the dissociation constant, corresponding to a sharp peak in association was seen when the binding affinity was plotted against antigen distance (Fig. 2, Supplementary Fig. 16). Binding became weaker when two antigens were arranged at short (3 nm) or long (17 nm) separations, and the binding affinity reached a striking maximum at 16 nm for all Abs studied. Monovalent binding was clearly resumed at 29 nm. Importantly, the results revealed differences between the IgG subclasses, where IgG1 and IgG4 showed similar behaviour, while IgG2, which is the most rigid subclass, showed a “stepwise” behaviour, where the binding affinity was similar at short distances but became significantly stronger at around 14-16 nm. In contrast, IgG3, which is the most flexible subclass, showed strong binding at shorter distances and even more so at 14-16 nm. Surprisingly, while the strongest binding was seen at 16 nm, there was a sharp drop in affinity when going to 17 nm (approx. 10-fold increase in K_D), indicating that this distance range around 16 nm is both optimal and at the same time close to the limiting distance for bivalent binding in the four human IgG subclasses. An artistic render of IgG1 stretched to 16 nm bivalent binding is shown in Fig. 1g.

To further explore the antigen binding properties of IgG3, and in particular the influence of its long hinge of 62 amino acids, we studied three hinge-engineered variants; one variant harbouring only the C terminal part of the hinge consisting of 15 amino acids (m15), one where the hinge is replaced with a short stretch of 5 amino acids (Ala-Ala-Ala-Cys-Ala) including a cysteine which makes a disulfide bridge between the heavy chains (HM4), and one lacking the hinge region altogether, such that the heavy chains are held together solely by non-covalent interactions in the CH3 domains and the CH2 domains are linked by a disulfide bridge at the C-terminal end of the light chains (HM5) (Supplementary Fig. 17). The results revealed that the HM4 mutant exhibited an IgG2-like behavior, with a strong preference for bivalent binding to antigens spaced in the 14-16 nm range, while the m15

mutant showed a binding behaviour similar to that of IgG1 and IgG4. This result is in line with what one would expect, given the length of the upper hinge and thus the flexibility of these mutants. Interestingly, IgG3 and both the HM4/HM5 mutants showed a peculiar behaviour with a local minimum in K_D around 3 nm. Importantly, we studied the binding behaviour of engineered monomeric IgM (C575S), which unlike its natural counterpart, does not form hexamers/pentamers. IgM does not contain a hinge region, but instead has an additional domain (Supplementary Fig. 1). Despite lacking a hinge region, we observed strong bivalent binding for antigen separations in the range of 3 to 17 nm (Fig. 2b, Supplementary Fig. 18), and the relatively low K_D at 29 nm (showing similar affinities as the IgGs displayed for 17 nm) indicates that to some extent, monomeric IgM is either able to stretch, perhaps by partial unfolding of domains, for bivalent binding well beyond 17 nm, or able to multimerize to reach long distances effectively (which would be consistent with the higher binding ratio seen in Fig. 2b). This remarkable ability of monomeric IgM to bind bivalently to antigens spaced over a wide range of distances, or *spatial tolerance*, may well be crucial for its special role in the first line of defence against pathogens as the IgM BCR is monomeric on the surface of B-cells.

Next, we explored the relationship between the binding affinity of the individual Fab and conformational flexibility of the anti-NIP Abs using the hapten NP as antigen instead of NIP, which gave 60-fold weaker K_D than that measured towards NIP conjugated nanostructures. We observed that the Abs failed to cross link two NP antigens by bivalent binding at all distances tested except the 16 nm distance for both IgG1 and IgG3 (Fig. 3). Thus, lower affinity antibodies clearly have a lower spatial tolerance than the stronger binders. Note that the Abs are identical (two different antigens are used) and flexibility arguments cannot explain the data, but instead suggest that the lower binding energy of the individual Fab arms are not strong enough to induce stretching or contraction of the arms, as may well be the case when binding to NIP.

Deconstruction of Multiple Antibody-Antigen Interactions

To deconstruct the complex interactions between multiple Abs and antigens, we designed pSPR experiments with nanoscale patterns of digoxigenin monomers, dimers, trimers, tetramers, pentamers as well as hexamers (brick structures, H1-6 hexagon with 15 nm edges, Fig. 4a, Supplementary Fig. 6) with the aim of constructing and empirically calibrating a model of multivalent binding dynamics. We measured both apparent affinity and average binding ratio (corresponding to average Abs per structure) using rabbit IgG (Fig. 4a, data in Supplementary Table 5). Notably, though tetramers and hexamers are engineered to enable a saturated state of bivalently bound Abs, we observed greater binding ratios than one would expect if this were to be the case. In contrast to single molecule methods, which have been employed to construct models of molecular dynamics according to individual trajectories26, we implemented a mathematical model that dissects the ensemble pSPR signal (four parameter continuous time Markov chain) that was able to accurately reproduce the binding curves from a bottom-up quantification of the contributions of internal molecular states (Fig. 4a-c). This dynamic model (detailed in Supplementary Note 2, Supplementary Fig. 20-32) assumes the local states: unoccupied, monovalently occupied, and bivalently occupied, and a network of transitions between those states mediated by the elementary processes:

monovalent attachment, monovalent detachment, monovalent-to-bivalent conversion, and bivalent-to-monovalent conversion. We sought a consensus set of the 4 rate parameters with which our model was able to produce satisfactory fits for all partial configurations of the hexamer antigen patterns (Supplementary Fig.24). Compared to earlier bivalent binding models27 that strive to accurately reproduce the dynamics of multivalent binding, our model can be used to predict the dynamics of binding to hypothetical antigen patterns of arbitrary geometry and provides data on internal conversion rates (Fig. 4c,e) and constituent microstates (Fig. 4b,e).

Hexameric antigen are of particular interest, as self-assembled Fc-Fc formed Ab hexamers that are monovalently bound to its antigens have been demonstrated to activate the complement system with high efficiency6. Our results show that the dominant interaction between an Ab and antigen hexamer patterns with 15 nm separations, is the engagement of bivalent binding of three Abs, and the probability of having six monovalently bound Abs is close to zero even at 0.5 nM Ab concentration (530 ppm among all possible microstates). However, the model of binding dynamics indicates that at steady state, Abs in every system assume a diverse distribution of states, dominated by bivalent saturation configurations (*e.g.* 3 bivalently bound Abs in the hexameric configuration). The probability space is shared with other complexes including mixtures of monovalent and bivalently bound Abs, driving the average occupancy to be greater than one would expect for bivalent saturation. This in turn explains the higher observed value for the binding ratio of antigen hexamer patterns (Fig. 4c-d, Supplementary Fig. 27i). Further, modelling can accurately predict that while about half of the hexamers are occupied by three Abs at high concentration (Fig. 4c-d) and settling fast at high concentration (Fig. 4d), a majority of the structures bear other patterns of bound Abs (Fig. 4c-d). Similar close examination of other Ab binding patterns also reveals a plethora of binding states where the most close-packed bivalent configurations do not in fact constitute a majority of the states even at higher Ab concentrations (Supplementary Figs. 26-32).

Conclusions

Here we reveal, using the pSPR method to measure Ab interactions with precise nanoscale patterns of antigens, that the reach necessary for bivalent antigen binding for human IgG subclasses ranges from approximately 3 nm to 17 nm, with a strong peak in binding affinity at 16 nm. In addition, we show that the Ab affinity has a large effect on the spatial tolerance for bivalent binding, in effect limiting bivalent binding to the 16 nm range for low affinity Abs. This relationship should be generalizable to the extent that if other factors such as configurational degrees of freedom are held constant, then we expect a reduction in the constituent epitope affinities to reduce the functional affinity or avidity as well. Spatial tolerance thus represents a capacity to endure affinity-weakening strain on binding sites28 in addition to reduction of that strain in the first place, e.g. via flexibility. We further find that differences in the Ab constant region appear to greatly influence binding strength to nanopatterns. IgG3 and, in particular monomeric IgM (present on naïve B-cells as BCR antigen receptor), have a much higher propensity for binding closely separated antigen pairs. This is in contrast to previous work on synthetic model systems suggesting a very modest effect of linker length and flexibility on bivalent binding strength29. In fact, our data is in line with recent studies indicating that the interaction of Ab with cognate antigen may be

affected by the constant region30 and that structural differences is sufficient to cause differences in binding between isotypes of BCRs31.

Monomeric IgM BCR, anchored to the membrane of naïve B cells in addition to IgD is typically the first to encounter a pathogen. The exceptional spatial tolerance for bivalent binding of human IgM uncovered in our data (3-29 nm, Fig. 2b) highlights an important feature of the structure of IgM. It suggests a unique ability to engage and dynamically interact with antigen patterns of a wide range of nanoscale densities as displayed by pathogens. As B cell responses mature in germinal centre reactions, less spatially tolerant isotypes such as IgG predominate. In addition to providing distinct effector functions to the antibodies, our data lead us to hypothesize that the IgG isotype switch is forcing the evolution of Abs that bind well despite having a lower spatial tolerance.

Further, by combining pSPR with a binding dynamics model, we dissect and characterize the distribution of Ab/antigen complexes, thereby providing a new basis for biophysical interrogation of these important interactions. From our study of the hexameric antigen patterns in particular, we hypothesize that the formation of hexameric IgG that has been shown to be important for complement activation6, might actually be promoted when an Ab has a low spatial tolerance but are present at a high concentration, as opposed to an Ab with higher spatial tolerance more likely to form bivalent attachments.

The immune response progression from IgM to lower spatially tolerant Abs such as IgG is consistent with such a hypothesis. Note that confidence and richness of state stratification obtained from the model is due to the extensive calibration through multiple antigen patterns. Reducing this information demand should be prioritized in future work, for example by utilizing more information-rich experimental data such as interferometric scattering microscopy (iSCAT)32. An expanded model (Supplementary Note 3), with the incorporation of experimentally determined binding rates as a function of antigen separation distance, can predict the most prevalent binding mode to arbitrary antigen patterns. Such analysis can provide mechanistic insights into how monoclonal Abs engage antigens displayed on pathogens. Given *a priori* knowledge about the antigen pattern on the target, the Ab type involved and the strength of the Ab-antigen interaction, one could predict how the Ab will engage the target, which pave the way for more systematic studies of how Abs with tailored antigen binding properties are able perform effector functions to eliminate infectious agents and cancer cells.

Online Methods

Preparation of the p7560 and p8634 scaffold for origami

A single colony of Escherichia coli JM109 was picked and transferred to 25 ml LB and cultured overnight at 37°C in a shaking incubator. 3 ml of the culture was diluted into 250 ml 2xYT, and cultured in the same shaking incubator. The phages (p7560 or p8634)17 were added to the bacteria culture when its optical density reaches 0.5 at a multiplicity of infection (MOI) of 1, and the whole culture was incubated for an additional 5 hr. The culture was transferred into a 250 ml centrifuge bottle and centrifuged twice at 4000 rcf for 25 mins 4°C, transferring into a fresh centrifuge bottle in between. 10g PEG 8000 and 7.5g NaCl was

added to the supernatant and was incubated in an ice water bath for 30min. The supernatant was then centrifuged at 10000 rcf for 30 mins 4°C, in this step the phages were pelleted. The phage pellet was then re-suspended in 10 ml Tris buffer (pH 8.5), added 10 ml of 0.2 M NaOH with 1% SDS, mixed gently by inversion and incubated for 3 min at room temperature. Afterwards, 7.5 ml of 3 M KOAc (pH 5.5) was added and the mixture was mixed gently by swirling, and incubated on ice for 10 min. The mixture was centrifuged at 16500 rcf for 30 min at 4°C, and the supernatant, which contains the M13 ssDNA, was added to 50 ml of 99.5% EtOH, mixed gently and incubated in an ice water bath for 30min before centrifuging at 16500 rcf for 30 min at 4°C. The DNA pellet was washed with 75% EtOH, and centrifuged again at 16500 rcf for 10 min 4oC. The pellet was dried at room temperature for a minimum of 15 min, and re-suspended in 10 mM Tris (pH 8.5). The concentration of the ssDNA was measured with NanoDrop, and the quality and purity were characterized by agarose gel electrophoresis (1.5 % w/v agarose gel with 0.5 mg/ml ethidium bromide in 0.5x TBE as running buffer).

Staple Oligonucleotide Preparation

Oligonucleotides were purchased from IDT (Belgium) in 96-well plates on a 25 nmol synthesis scale. The staples in each well were ordered to be diluted in water to a final concentration of 100 μM. The final concentration of the staples after pooling was adjusted to 400 nM each. NIP-, NP- and Biotin-modified oligos were purchased from IDT.

Preparation of antigen decorated nanostructures

Structures were designed using caDNAno33. The 18HB has been characterized earlier34–36. The standard folding conditions used in this study were as follows: 20 nM ssDNA scaffold, 100 nM each staple oligonucleotide, 13 mM MgCl2, 5 mM Tris pH 8.5, and 1 mM EDTA. Folding was carried out by rapid heat denaturation followed by slow cooling from 80 to 60 °C over 20 min, then 60 to 24 °C for 14 h. Removal of excess staples was done by washing (repetitive concentration/dilution) the 18HB with PBS pH 7.4 supplemented with 10 mM MgCl2 in 100 kDa MWCO 0.5 mL Amicon centrifugal filters (Merck Millipore).

Uncertainty estimation of distances

All double site distances (i.e. all except the “0” nm) have variations coming from the linker length of 2 NT, and from variations of the structures as a whole. The structural variations of the 18HB used for these experiments have been thoroughly characterized in earlier work36. From these earlier measurements we found that the structures can vary in length due to bending and other variations with a standard deviation of 3% of the total length. The linkers additionally, constitute entropic springs centred around the mean distances with a maximum extension at each site of approximately 2 nm, and thus x±4 nm for a two-site distance, where x is the mean antigen separation. The variance of a uniform distribution with a 4 nm spread is 42/12 nm^2 and the standard deviations used for the plots are calculated as the square root of the sum of these variances: $\sigma(x)$ nm = $\sqrt{(42/12 + (0.03x)^2)}$.

Europe PMC Funders Author Manuscripts

Preparation of streptavidin CM3 sensor chip for SPR

A BIAcore t200 (GE Healthcare) was used to measure the binding kinetics of the antibody-antigen pairs. Streptavidin (Sigma Aldrich) was dissolved in 100 mM sodium acetate buffer, pH 4.5, and immobilized on a CM3 chip (GE Healthcare) according to manufacturer instructions. Biotinylated anchor oligonucleotide was adjusted to 200 nM in HBS-EP+ running buffer, and passed through the SPR surface for 20 mins, followed by a 5 min 50 mM NaOH washing.

SPR Kinetic Experiments

Streptavidin (10 μg/ml in 10 mM NaOAc pH 4.5) was immobilized to a CM3 sensor chip (GE Healthcare, Sweden) via NHS/EDC coupling, the running buffer used here is 1xHBS-EP (GE Healthcare, Sweden). Biotinylated anchor oligonucleotides (200 nM diluted in 1x HBS-EP running buffer) was injected over the surface for 20 minutes, followed by in short 5 minutes injection of 50 mM NaOH to wash away non-specifically bound oligos. The DNA nanostructures carrying the antigen patterns (prepared in 1x PBS supplemented with 10 mM MgCl2) were injected over the streptavidin – biotin anchor oligo surface for 20 mins, followed by a 10 min buffer wash. Abs were diluted to various concentration ranges, depending on its affinity towards its antigen (0.025 – 0.5 nM for anti-digoxigenin Abs and 1-50 nM for anti-biotin Abs, 0.0256-1 nM for anti-NIP Abs). A single cycle kinetics injection was used to inject the increasing concentrations of the Abs, with each concentration having a 3 to 5 mins contact time and 30 μl/min flow rate to avoid mass-transfer limitations, and after the highest concentration, the dissociation curved was recorded for 15 mins. All antibody kinetics experiments with DNA origami patterns were carried out with 1x HBS-EP running buffer supplemented with 10 mM MgCl2. The t200 evaluation software was used to fit the data to a 1:1 Langmiur binding model and calculate the ka, kd, KD and binding capacity. The surface was regenerated with 5 min injection of 50 mM NaOH.

Transmission electron microscopy

5 ul 10 nM of purified DNA nanostructures were spotted on glow-discharged, carbon-coated Formvar grids (Electron microscopy sciences) and incubated for 20 seconds before blotting of with filter paper, the grid was immediately stained with 2% (w/v) uranyl formate solution for 20s and finally blotting of the solution. The grids were then imaged with an FEI Morgagni 268(D) transmission electron microscope.

Gel electrophoresis

The DNA origami nanostructures were loaded (64 pmole) in 2% agarose gels containing 0.5 mg/ml ethidium bromide, and the gel was ran at 70V for 3.5 hr in an ice water bath. The gels were imaged with ImageQuant LAS 4000 (GE Healthcare).

Computational Model

Detailed mathematical steps are described in the supplementary materials and methods. The model is a continuous time Markov chain based on a chemical reaction network37,38 constructed from decomposing the antibody binding on an arbitrary 2D antigen pattern into

four elementary processes (monovalent binding, monovalent un-binding, monovalent to bivalent conversion, and bivalent to monovalent conversion). A breadth first search algorithm39,40 was executed then for a given antigen pattern to discover the set of states (i.e. every combination of empty antigens, monovalently-occupied antigens, and bivalently occupied antigens possible for a given pattern) and the transitions (each mediated by one of the four processes above) between those states. SPR kinetic profiles were generated by computing the structure's probability to occupy a given state at each point in time beginning from an initial condition on the basis of rates (four in total, each corresponding to one of the elementary processes, parameters to be fit to experiment) determining the flux of state probabilities occurring from one time step to the next41,42. Each state has a corresponding occupancy, or number of bound Abs, associated with it that are weighted by the probability of the state to then obtain the average occupancy per structure. Experimental profiles were normalized to the number of structures allowing us to fit simulated binding curves to experimental curves and estimate values of the four rate parameters through minimization of sum the of squared errors. All computations were implemented with custom code written in Python (see supplementary data).

Code availability

All the code used for the computational results is available upon request.

Materials

All BIAcore products were purchased from GE Healthcare (Sweden). All Abs used in this study are monoclonal. Rabbit anti-digoxigenin IgG (#9H27L19) was purchased from Thermo Scientific (Sweden); Mouse anti-digoxigenin IgG1 (#ab420) was purchased from Abcam (UK); Mouse anti-biotin IgG1 (#ab201341 and # ab46862) were purchased from Abcam (UK). Reagents for buffers and solutions (PBS, NaOH, and MgCl2) were purchased from Sigma-Aldrich.

Production and purification of anti-NIP Abs

Vectors encoding the constant heavy chains of human IgG1, IgG2, IgG3, IgG3, and IgG3 hinge engineered variants and monomeric IgM (C575S) with specificity for the hapten 5-iodo-4-hydroxy-3-nitro-phenacetyl (NIP) as well as a vector encoding the mouse λ light chain with NIP specificity have previously been described43–47. The Abs were produced in HEK293E cells (ATCC, CRL-1573) by transient co-transfection of the heavy and light chain encoding vectors using Lipofectamine 2000 (Invitrogen) following the manufacturer's instructions or by stably transfected J558L cell lines. The Abs were purified from collected supernatants and purified using a column coupled with 4-hydroxy-3-nitrophenyl acetyl or a CaptureSelectTM pre-packed anti-hIgG-CH1 column (Life Technologies) as described by the manufacturer. The collected proteins were up-concentrated and buffer-changed to PBS (Sigma-Aldrich) using Amicon Ultra-15 ml 50K columns (Millipore) prior to size exclusion chromatography using a Superdex 200 increase 10/300 GL column (GE Healthcare) coupled to an ÄKTA FPLC instrument (GE Healthcare). The monomeric fractions were up-concentrated by Amicon Ultra-0.5 ml 100K columns (Millipore). The HEK293E cell line and J558L murine myeloma cell lines were maintained in RPMI (Sigma-Aldrich,) and

supplemented with supplemented with 10% heat-inactivated FCS 25 μg/ml streptomycin and 25 U/ml penicillin.

Supplementary Material

Refer to Web version on PubMed Central for supplementary material.

Acknowledgments

This work was funded through grants from the Swedish Research Council (grant 2013-5883 to B.H.), the Swedish Foundation for Strategic Research (grant FFL12-0219 to B.H.), the European Research Council (ERC) under the European Union's Horizon 2020 research and innovation programme (grant agreement no 724872 to B.H.) and the Knut and Alice Wallenberg foundation (Academy Fellow grant KAW2014.0241 to B.H.). The SPR instrument was funded by the SFO initiative StatRegen at Karolinska Institutet. J.T.A. was in part supported by the Research Council of Norway through its Centres of Excellence funding scheme (project number 179573) and the Research Council of Norway (Grant no. 230526/F20 and 179573/V40). We thank Stian Foss for help with schematic antibody figures. We thank Yenan Bryceson and Samuel Chiang for work on experimental testing and valuable discussions, and Gunilla Karlsson Hedestam and Ana Teixeira for valuable discussions.

References

1. Bachmann MF, Jennings GT. Vaccine delivery: a matter of size, geometry, kinetics and molecular patterns. Nat Rev Immunol. 2010; 10:787–796. [PubMed: 20948547]
2. Martinez-Murillo P, et al. Particulate Array of Well-Ordered HIV Clade C Env Trimers Elicits Neutralizing Antibodies that Display a Unique V2 Cap Approach. Immunity. 2017; 46:804–817.e7. [PubMed: 28514687]
3. Kanekiyo M, et al. Self-assembling influenza nanoparticle vaccines elicit broadly neutralizing H1N1 antibodies. Nature. 2013; 499:102–106. [PubMed: 23698367]
4. Preiner J, et al. IgGs are made for walking on bacterial and viral surfaces. Nat Commun. 2014; 5:4394. [PubMed: 25008037]
5. Maity PC, et al. B cell antigen receptors of the IgM and IgD classes are clustered in different protein islands that are altered during B cell activation. Sci Signal. 2015; 8:ra93. [PubMed: 26373673]
6. Diebolder, Ca; , et al. Complement is activated by IgG hexamers assembled at the cell surface. Science (80-.). 2014; 343:1260–3.
7. Sondermann P, Huber R, Oosthuizen V, Jacob U. The 3.2-A crystal structure of the human IgG1 Fc fragment-Fc gammaRIII complex. Nature. 2000; 406:267–273. [PubMed: 10917521]
8. Baker K, et al. Neonatal Fc receptor for IgG (FcRn) regulates cross-presentation of IgG immune complexes by CD8-CD11b+ dendritic cells. Proc Natl Acad Sci. 2011; 108:9927–9932. [PubMed: 21628593]
9. Qiao S-W, et al. Dependence of antibody-mediated presentation of antigen on FcRn. Proc Natl Acad Sci. 2008; 105:9337–9342. [PubMed: 18599440]
10. Saphire EO. Crystal Structure of a Neutralizing Human IgG Against HIV-1: A Template for Vaccine Design. Science (80-.). 2001; 293:1155–1159.
11. Bruhns P, et al. Specificity and affinity of human Fc receptors and their polymorphic variants for human IgG subclasses. Blood. 2009; 113:3716–3725. [PubMed: 19018092]
12. Tian X, et al. In-depth analysis of subclass-specific conformational preferences of IgG antibodies. IUCrJ. 2015; 2:9–18.
13. Smith TJ, Olson NH, Cheng RH, Chase ES, Baker TS. Structure of a human rhinovirus-bivalently bound antibody complex: implications for viral neutralization and antibody flexibility. Proc Natl Acad Sci U S A. 1993; 90:7015–7018. [PubMed: 8394005]
14. Zhang X, et al. 3D Structural Fluctuation of IgG1 Antibody Revealed by Individual Particle Electron Tomography. Sci Rep. 2015; 5:9803. [PubMed: 25940394]
15. Luedtke R, Owen CS, Karush F. Proximity of antibody binding sites studied by fluorescence energy transfer. Biochemistry. 1980; 19:1182–1192. [PubMed: 7189409]

16. Seeman NC, Sleiman HF. DNA nanotechnology. Nat Rev Mater. 2017; 3:17068.
17. Rothemund PWK. Folding DNA to create nanoscale shapes and patterns. Nature. 2006; 440:297–302. [PubMed: 16541064]
18. Douglas SM, et al. Self-assembly of DNA into nanoscale three-dimensional shapes. Nature. 2009; 459:414–418. [PubMed: 19458720]
19. Benson E, et al. DNA rendering of polyhedral meshes at the nanoscale. Nature. 2015; 523:441–444. [PubMed: 26201596]
20. Steinhauer C, Jungmann R, Sobey TL, Simmel FC, Tinnefeld P. DNA origami as a nanoscopic ruler for superresolution microscopy. Angew Chemie - Int Ed. 2009; 48:8870–8873.
21. Nickels PC, et al. Molecular force spectroscopy with a DNA origami-based nanoscopic force clamp. Science. 2016; 354:305–307. [PubMed: 27846560]
22. Fu J, et al. Multi-enzyme complexes on DNA scaffolds capable of substrate channelling with an artificial swinging arm. Nat Nanotechnol. 2014; 9:531–536. [PubMed: 24859813]
23. Wollman AJM, Sanchez-Cano C, Carstairs HMJ, Cross RA, Turberfield AJ. Transport and self-organization across different length scales powered by motor proteins and programmed by DNA. Nat Nanotechnol. 2013; 9:44–47. [PubMed: 24213281]
24. Funke JJ, Dietz H. Placing molecules with Bohr radius resolution using DNA origami. Nat Nanotechnol. 2015; 11:47–52. [PubMed: 26479026]
25. Rinker S, Ke Y, Liu Y, Chhabra R, Yan H. Self-assembled DNA nanostructures for distance-dependent multivalent ligand-protein binding. Nat Nanotechnol. 2008; 3:418–422. [PubMed: 18654566]
26. McKinney SA, Joo C, Ha T. Analysis of Single-Molecule FRET Trajectories Using Hidden Markov Modeling. Biophys J. 2006; 91:1941–1951. [PubMed: 16766620]
27. Müller KM, Arndt KM, Plückthun A. Model and Simulation of Multivalent Binding to Fixed Ligands. Anal Biochem. 1998; 261:149–158. [PubMed: 9716417]
28. Natkanski E, et al. B Cells Use Mechanical Energy to Discriminate Antigen Affinities. Science (80-.). 2013; 340:1587–1590.
29. Mack ET, Snyder PW, Perez-Castillejos R, Whitesides GM. Using Covalent Dimers of Human Carbonic Anhydrase II To Model Bivalency in Immunoglobulins. J Am Chem Soc. 2011; 133:11701–11715. [PubMed: 21671600]
30. Sela-Culang I, Kunik V, Ofran Y. The structural basis of antibody-antigen recognition. Front Immunol. 2013; 4:1–13. [PubMed: 23355837]
31. Übelhart R, et al. Responsiveness of B cells is regulated by the hinge region of IgD. Nat Immunol. 2015; 16
32. Cole D, Young G, Weigel A, Sebesta A, Kukura P. Label-Free Single-Molecule Imaging with Numerical-Aperture-Shaped Interferometric Scattering Microscopy. ACS photonics. 2017; 4:211–216. [PubMed: 28255572]
33. Douglas SM, et al. Rapid prototyping of 3D DNA-origami shapes with caDNAno. Nucleic Acids Res. 2009; 37:5001–6. [PubMed: 19531737]
34. Shaw A, et al. Spatial control of membrane receptor function using ligand nanocalipers. Nat Methods. 2014; 11:841–6. [PubMed: 24997862]
35. Zhao Y-X, et al. DNA origami delivery system for cancer therapy with tunable release properties. ACS Nano. 2012; 6:8684–91. [PubMed: 22950811]
36. Reuss M, et al. Measuring true localization accuracy in super resolution microscopy with DNA-origami nanostructures. New J Phys. 2017; 19
37. Gillespie DT. Exact stochastic simulation of coupled chemical reactions. J Phys Chem. 1977; 81:2340–2361.
38. Kurtz TG. The Relationship between Stochastic and Deterministic Models for Chemical Reactions. J Chem Phys. 1972; 57:2976.
39. Moore, EF. Proceedings of the International Symposium on the Theory of Switching. Harvard University Press; 1959. The shortest path through a maze; 285–292.
40. Lee CY. An Algorithm for Path Connections and Its Applications. IRE Trans Electron Comput. 1961; EC-10:346–365.

41. Fox BLW, Glynn P. Computing Poisson Probabilities. Commun ACM. 1988; 31:440–445.
42. Gross D, Miller DR. The Randomization Technique as a Modeling Tool and Solution Procedure for Transient Markov Processes. Oper Res. 1984; 32:343–361.
43. Michaelsen TE, Garred P, Aase A. Human IgG subclass pattern of inducing complement-mediated cytolysis depends on antigen concentration and to a lesser extent on epitope patchiness, antibody affinity and complement concentration. Eur J Immunol. 1991; 21:11–16. [PubMed: 1703960]
44. Norderhaug L, Olafsen T, Michaelsen TE, Sandlie I. Versatile vectors for transient and stable expression of recombinant antibody molecules in mammalian cells. J Immunol Methods. 1997; 204:77–87. [PubMed: 9202712]
45. Berntzen G, et al. Prolonged and increased expression of soluble Fc receptors, IgG and a TCR-Ig fusion protein by transiently transfected adherent 293E cells. J Immunol Methods. 2005; 298:93–104. [PubMed: 15847800]
46. Michaelsen TE, et al. One disulfide bond in front of the second heavy chain constant region is necessary and sufficient for effector functions of human IgG3 without a genetic hinge. Proc Natl Acad Sci U S A. 1994; 91:9243–7. [PubMed: 7937748]
47. Brekke OH, Michaelsen TE, Sandin R, Sandlie I. Activation of complement by an IgG molecule without a genetic hinge. Nature. 1993; 363:628–630. [PubMed: 8510754]
48. Kirnbauer R, Booy F, Cheng N, Lowy DR, Schiller JT. Papillomavirus L1 major capsid protein self-assembles into virus-like particles that are highly immunogenic. Proc Natl Acad Sci U S A. 1992; 89:12180–4. [PubMed: 1334560]
49. McAleer WJ, et al. Human hepatitis B vaccine from recombinant yeast. Nature. 1984; 307:178–180. [PubMed: 6318124]
50. Vreden SG, Verhave JP, Oettinger T, Sauerwein RW, Meuwissen JH. Phase I clinical trial of a recombinant malaria vaccine consisting of the circumsporozoite repeat region of Plasmodium falciparum coupled to hepatitis B surface antigen. Am J Trop Med Hyg. 1991; 45:533–8. [PubMed: 1835311]
51. King NP, et al. Computational Design of Self-Assembling Protein Nanomaterials with Atomic Level Accuracy. Science (80-.). 2012; 336:1171–1174.
52. Edeling MA, et al. Potent Dengue Virus Neutralization by a Therapeutic Antibody with Low Monovalent Affinity Requires Bivalent Engagement. PLoS Pathog. 2014; 10
53. Lee PS, et al. Receptor mimicry by antibody F045-092 facilitates universal binding to the H3 subtype of influenza virus. Nat Commun. 2014; 5:3614. [PubMed: 24717798]
54. Mouquet H, et al. Polyreactivity increases the apparent affinity of anti-HIV antibodies by heteroligation. Nature. 2010; 467:591–595. [PubMed: 20882016]
55. Galimidi RP, et al. Intra-spike crosslinking overcomes antibody evasion by HIV-1. Cell. 2015; 160:433–446. [PubMed: 25635457]
56. Harris LJ, et al. The three-dimensional structure of an intact monoclonal antibody for canine lymphoma. Nature. 1992; 360:369–72. [PubMed: 1448155]
57. Harris LJ, Skaletsky E, McPherson A. Crystallographic structure of an intact IgG1 monoclonal antibody. Wilson IA. J Mol Biol. 1998; 275:861–872. [PubMed: 9480774]
58. Guddat LW, Herron JN, Edmundson AB. Three-dimensional structure of a human immunoglobulin with a hinge deletion. Proc Natl Acad Sci U S A. 1993; 90:4271–5. [PubMed: 8483943]
59. Vidarsson G, Dekkers G, Rispens T. IgG Subclasses and Allotypes: From Structure to Effector Functions. Front Immunol. 2014; 5
60. Müller R, et al. High-resolution structures of the IgM Fc domains reveal principles of its hexamer formation. Proc Natl Acad Sci U S A. 2013; 110:10183–8. [PubMed: 23733956]
61. Mandelboim O, et al. Human CD16 as a lysis receptor mediating direct natural killer cell cytotoxicity. Proc Natl Acad Sci U S A. 1999; 96:5640–4. [PubMed: 10318937]
62. Retra K, Irth H, Van Muijlwijk-Koezen JE. Surface Plasmon Resonance biosensor analysis as a useful tool in FBDD. Drug Discov Today Technol. 2010; 7:e181–e187.

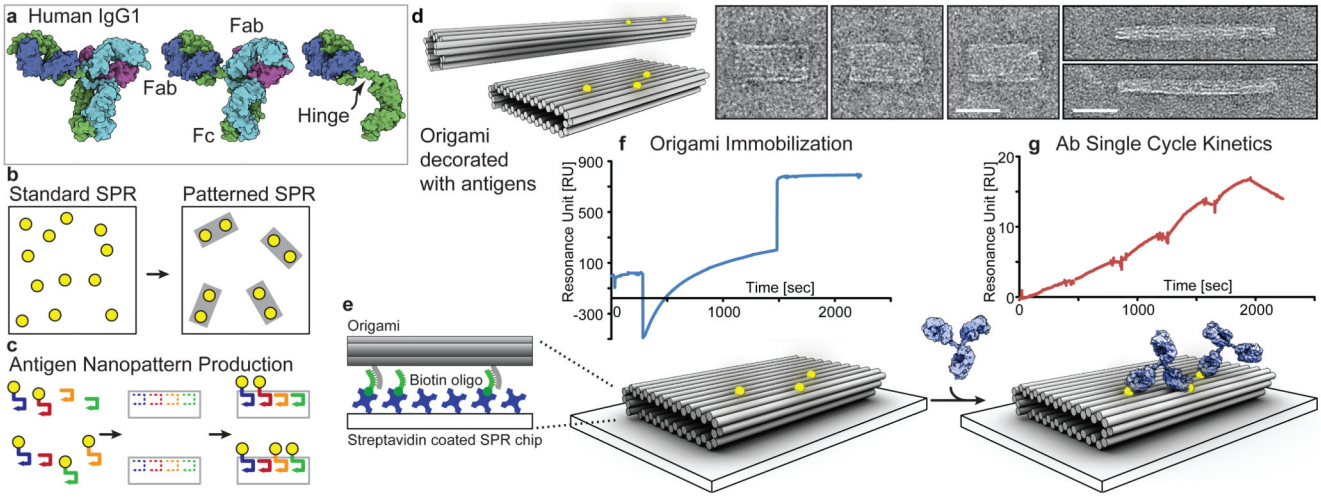

Fig. 1. The Patterned Surface Plasmon Resonance method.

a 3D rendering of human IgG1 based on X-ray crystallography data (PDB:1HZH).10 **b** The advantage of pSPR: in contrast to conventional SPR, which randomly arranges its ligands on the surface, the pSPR method utilizes DNA origami to pre-pattern the antigen of interest (yellow dots) prior to immobilization. **c** Fabrication of antigen nanopatterns: antigen nanopatterns were fabricated using different combinations of antigen-decorated staple oligonucleotides (different coloured lines). **d** 3D models and TEM images of the antigen nanopatterns: 3D models (left) using cylinders as a representation of double helices and TEM negative stain micrographs (right) with 40 nm scale bars of the DNA nanostructures used in this study. Two types of DNA nanostructures, a 18-helix rod and a 44-helix brick, were used to pattern antigens. **e-f** pSPR experimental workflow: the antigen nanopatterns were immobilized onto a streptavidin-biotinylated oligonucleotide surface via oligo hybridization to sequences protruding from the bottom of the origami, followed by an injection of increasing antibody concentrations, **g**, and finally a dissociation phase and the kinetic data can be obtained by fitting the binding curves with a 1:1 binding model (See Supplementary Fig.7). Model showing origami and antibody renders to scale, illustrating a 16 nm bivalent binding and a monovalent binding.

Europe PMC Funders Author Manuscripts

Europe PMC Funders Author Manuscripts

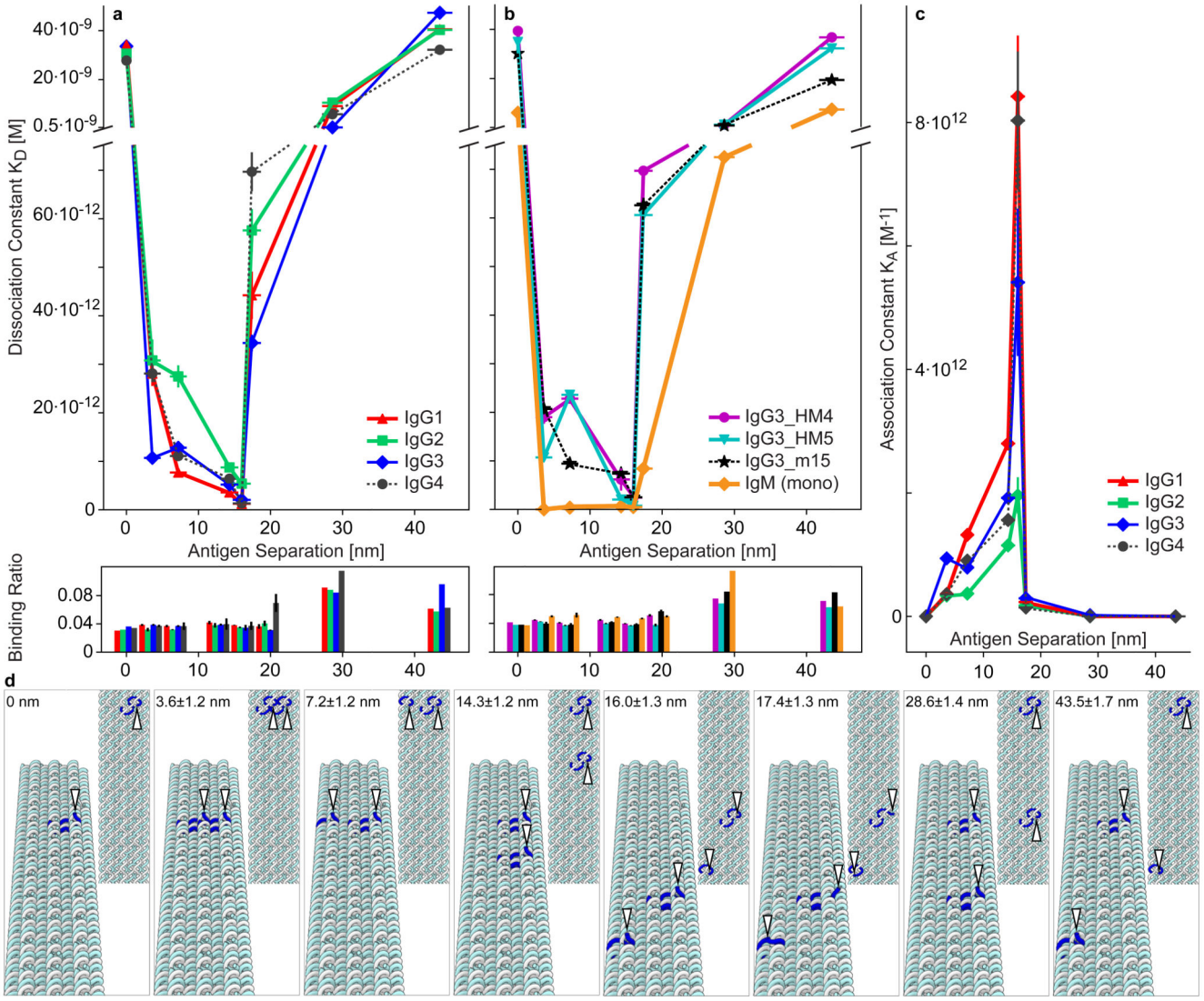

Fig. 2. Ab binding to precise antigen separations.

Human anti-NIP Abs binding to two NIP molecules patterned on the 18HB at varying separations. **a-b** Scatter graphs of K_D and binding ratio (response units (RU):Abs / RU:structures, which correspond to average Abs per structure) for the various separations. See **e** and Fig S5 for exact structure designs. The "0" distance is just one displayed antigen. The y-axis (top parts) is the apparent binding affinity recorded and fitted with BIAcore t200 evaluation software. The amount of Ab 1 RU of structure can bind to is plotted in the bottom panels (binding ratio). **a** Data for all wt IgG subclasses. **b** Data for IgG3 hinge mutants and monomeric IgM. **c** The same data as in A plotted as association constants, K_A (=1/K_D), vs. separations for the IgG subclasses. A peak behaviour in the changes of K_A was observed for all tested Abs, the bivalent binding becomes weaker at short (3-7 nm) and long (17 nm) distances, and this behaviour varies between different Ab subclasses. (n=3 or 4, detailed description is given in Supplementary Table 4; central values = average value; y error bars = standard error of mean, sometimes smaller than the markers; For samples without error bars

n =1). Distance *i.e.* x-error bars are standard deviations from a uniform ±2 nm distribution added to a 3% standard deviation derived from structure fluctuations of the 18HB, see methods. **d** Zoomed in renders (top and perspective views) of the 18HB showing the locations of the NIP modified staple-oligos in blue, NIP locations highlighted with white arrowheads. The distances are shown as the design distance ± distance error calculated as described in methods.

Europe PMC Funders Author Manuscripts

Europe PMC Funders Author Manuscripts

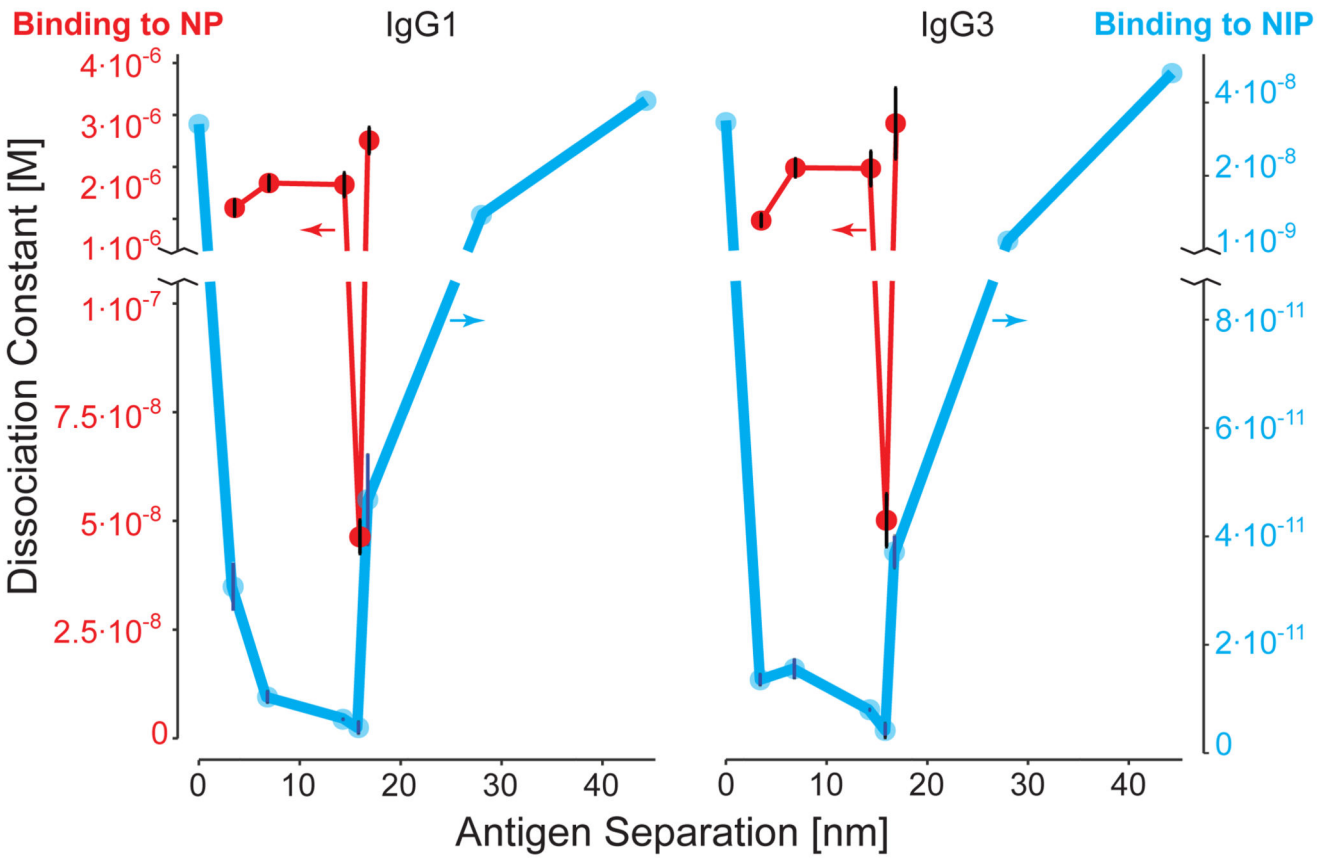

Fig. 3. Spatial tolerance is lower in low affinity Abs.

A comparison of human anti-NIP IgG1 and IgG3 binding to NIP or NP. The x-axis is the separation distance between two antigens. See, Fig. 2 and Supplementary Fig. 6 for exact structure designs. The point at 0 represents a structure with one antigen. NIP data points are identical to that of Fig. 2, and their binding affinities correspond to the right, blue, y-axis. NP binding affinity (KD) is plotted on the red, left, y-axis. (n=3; central values = average value; error bars = standard error of mean. For samples without error bars n =1)

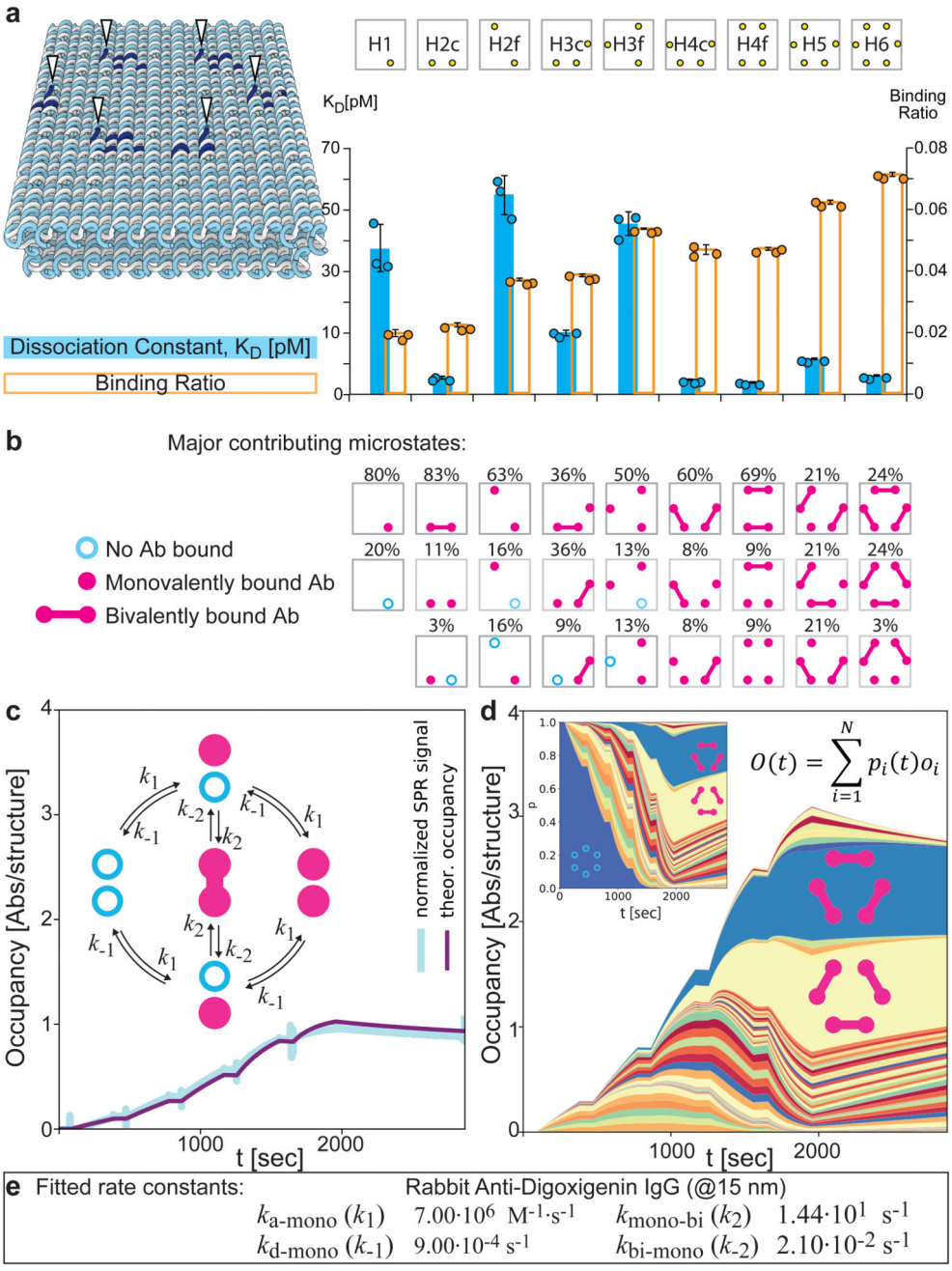

Fig. 4. Steady state and dynamic analyses of multivalent patterns reveals a binding profile stratified by competing states.

a Comparison of final measured binding ratio (orange secondary y axis) and apparent K_D values (blue main y axis) determined for different nanopatterns (top row schematics, H-hexagon, #-no of antigens displayed, c-close, f-far) of digoxigenin on the brick structure (left) where antigens are displayed in a regular hexagon with edge distances of approximately 15 nm (Fig. 1, Supplementary Fig. 5) using rabbit IgG. (n=3; central values = average value; error bars = standard deviation) **b** Their corresponding most-dominant

Europe PMC Funders Author Manuscripts

microstates determined by a model of steady state binding behaviour. **c.** example of SPR curve (cyan) for a partial hexamer configuration (H2c in **a**) and corresponding fitted model output (magenta). Inset shows schematic visualization of the network of states for this system and transitions between those states governed by the 4 rate parameters. **d** Weighted probability trajectory for the hexameric antigen pattern. Each state has a corresponding occupancy, which can be used to weight its probability according to its contribution to the SPR signal. The stacked summation of all weighted probabilities reproduces the SPR curve for that experiment. Equation describes total occupancy as the expectation value function of individual state occupancies. Inset shows the unweighted probability distribution of states including the empty state initial condition in blue. **e** Rate constants, including internal monovalent-bivalent kinetics determined by model fitting for rabbit IgG using data from binding to the brick patterns.

Europe PMC Funders Author Manuscripts